Journal of Materials Chemistry A

Accepted Manuscript

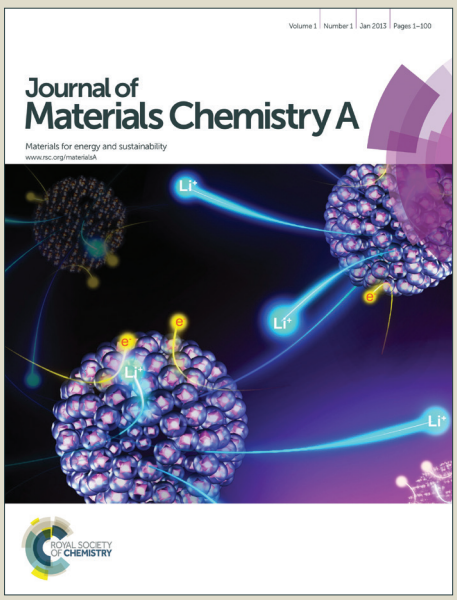

ROYAL SOCIETY OF CHEMISTRY

www.rsc.org/materialsA

The dynamic degradation of Al anode in solid-state batteries is quantitatively measured by combining real-time scanning electron microscopy with electrochemical cycling.

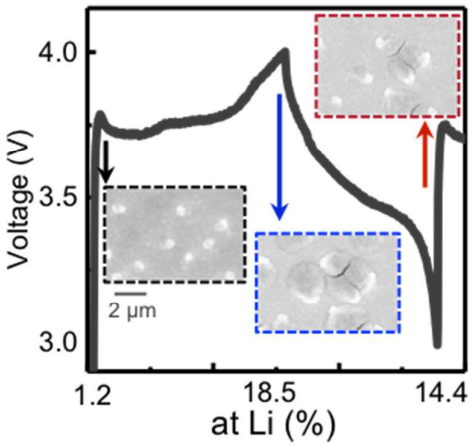

Journal Name

RSCPublishing

ARTICLE

Insights into capacity loss mechanisms of all-solid-state Li-ion batteries with Al anodes

Cite this: DOI: 10.1039/x0xx00000x

Marina S. Leite[1,,2,3*], Dmitry Ruzmetov[2,3], Zhipeng Li[4], Leonid A. Bendersky[4], Norman C. Bartelt[5] Andrei Kolmakov[2], and A. Alec Talin[2,5*]

Received 00th January 2012,
Accepted 00th January 2012

DOI: 10.1039/x0xx00000x

www.rsc.org/

The atomistic mechanisms for lithiation/delithiation in all-solid-state batteries is still an open question, and the 'holy grail' to engineer devices with extended lifetime. Here, by combining real-time scanning electron microscopy in ultra-high vacuum with electrochemical cycling, we quantify the dynamic degradation of Al anode in Li-ion all-solid-state batteries, a promising alternative for ultra lightweight devices. We find that AlLi alloy mounds are formed on the top surface of the Al anode and that degradation of battery capacity occurs because of Li trapped in them. Our approach establishes a new platform for probing the real-time degradation of electrodes, and can be expanded to other complex system, allowing for high throughput characterization of batteries with nanoscale resolution.

Introduction

Increasing the capacity of Li-ion batteries remains a critical technological challenge given the increasingly pervasive use of electrochemical energy storage in portable electronics, transportation, and the electric grid.[1-5] Li alloy electrodes are attractive due to their high capacity, but suffer large volumetric expansion/contraction during lithiation/de-lithiation, which can lead to fracture and pulverization of the anode material.[6,7,8] This failure mechanism can be mitigated in Si nanostructures and thin films by reducing the diameter or thickness to below ~100 nm, which allows the material to better accommodate lithiation/de-lithiation strains without fracture.[9] In contrast to Si, Hudak *et al.* observed that Al nanowires and films exhibited a reverse trend: smaller diameter nanowires and thinner films degraded more rapidly compared to similar structures with larger critical dimensions.[7, 10] This effect was attributed in part to the rapid loss of electrical conductivity due to pulverization in small structures. Ichitsubo *et al.* have also recently investigated lithiation of Al anodes and suggested that the large strain energy associated with AlLi formation inside the Al matrix retarded the kinetics of lithiation/de-lithiation sufficiently to effectively arrest the reaction.[11, 12]

Here, we combine real-time scanning electron microscopy (SEM) and Auger electron spectroscopy (AES) under ultra-high vacuum conditions with electrochemical cycling to understand the dynamic degradation of the Al anode upon charging/discharging of a thin film, all-solid-state Li-ion battery (TFLIB) with a $LiCoO_2$ cathode and N-doped $LiPO_4$ (LiPON) electrolyte. *In situ* transmission electron microscopy (TEM) experiments have been previously performed with both Si and Al single nanowire anodes.[6,7] Although highly informative, the morphology evolution captured in single nanowire electrode studies may not be representative of larger macroscopic systems due to size scaling of material mechanical properties and surface effects, as well as due to uncertainties in the location of active electrolyte/electrode interfaces. Furthermore, electrochemical experiments with individual nanostructures under strict galvanostatic control are highly challenging because they operate at very small currents. Using an all-solid state battery compatible with an ultra-high vacuum environment and electron beam based imaging and spectroscopic tools, we were able to precisely control the lithiation rate, the battery state-of-charge and state-of-discharge (SOC and SOD, respectively), record the electrochemical potential, and to correlate these parameters with specific changes in the electrode morphology and chemical composition. An additional motivation for investigating TFLIBs with Al anodes is that compared to Li which melts at 165 ^{o}C, the higher melting point of Al makes it more attractive for 'on-chip' energy storage applications. In addition, the high conductivity, higher melting point (relative to Li), low cost, and compatibility with complementary metal–oxide–semiconductor (CMOS) processing, make Al an attractive replacement to the currently used thin film Li anodes in all solid state batteries for on-chip integrated microbatteries.

However, we find that these batteries lose 90% of their capacity after 100 cycles. An explanation to the source of the capacity loss is provided by our observation that Li predominately reacts with Al on the anode surface rather than at the anode-electrolyte interface. This surface reaction leads to significant changes in the Al film morphology during lithation. With increasing number of cycles, the smooth surface of the Al films (typical grain size ≈200 nm, and root mean square roughness of ≈20 nm) becomes covered with quarter-micron high AlLi mounds. The loss in battery capacity is directly related to the gradual irreversible Li trapping in these formations. Remarkably these mounds remain in electrical contact with the bulk

Al anode. This is inconsistent with the common assumption that capacity loss in reactive anodes that experience large strains during lithiation is due to pulverization and degradation of electrical contact.[13] We postulate that the origin of the capacity fade is due to the blockage of Li and Al diffusion pathways necessary for the decomposition of AlLi at room temperature and which occurs as a result of Li-Al-O formation on exposed Li-Al surfaces inside the porous mounds.

Experimental section

All solid-state battery fabrication

The samples were fabricated on a Si (001) substrate with a 100 nm thick SiO_2 layer. 20 nm of Ti and 120 nm of Pt, or a sequential deposition of Ti(30nm) / Pt(90 nm) / Ti(40 nm) / Pt(100 nm) / Ti(80 nm) were used as the bottom contact for current collection. 305 nm of crystalline $LiCoO_2$ (cathode) was deposited by sputtering in the same chamber and without exposure to air. The sample was then annealed in ambient oxygen at 700 ^oC for 2 h to smooth the cathode layer.[14] Following the heat treatment, the sample was sputter coated with 365 nm of LiPON (electrolyte) and finally 400 nm of Al anode. Batteries with 0.51 mm in diameter were fabricated by using a stainless steel shadow mask for the anode deposition.

In situ SEM measurements

The *in situ* electrochemical measurements were performed under ultra-high vacuum conditions at 8.0×10^{-8} Pa (6×10^{-10} Torr) using a tungsten probe as the top current collector and the sample stage as the bottom contact. A current-voltage generator was used to charge the device. Simultaneously, all the *in situ* SEM images were acquired using a 5 kV, 100 pA electron beam and an in-lens detector.

Ex situ TEM and SEM measurements

Cross-sectional transmission electron microscope (TEM) thin film samples were prepared by focused ion beam technique. Initially, we deposited 2 µm of Pt as a protective layer. A representative region of the sample was lifted-off and glued to a cross-sectional Cu TEM grid. Finally, the sample was thinned to electron beam transparent thickness. High spatial resolution imaging and micro- or chemical-analysis were performed with an analytical TEM, operating at 300 kV accelerating voltage with 3.8 kV extraction voltage. The system is also equipped with a 3000 high-angle annular dark-field (HAADF) detector and a lithium-drifted silicon energy dispersive X-ray spectrometer. The *ex situ* SEM measurements were acquired using a 5.0 kV electron beam, 50 pA beam current, and two types of secondary electron detectors: through-the-lens (TLD) and ion imaging (ICE).

In situ Auger electron spectroscopy:

AES measurements were performed *in situ* before, during and after lithiation cycles. The electron beam incident angle and take-off angle to analyzer were 25 ° and 35 ° correspondingly with respect to the sample normal. AES spectra were collected via rastering over 2×10^3 μm^2 areas, using 1 nA and 3 keV (or 7 keV) electron. The sputtering was done inside the same chamber using 2 keV Ar ions for shallow (tens of nanometers) and deep (hundreds of nanometers) etching.

Results and discussion

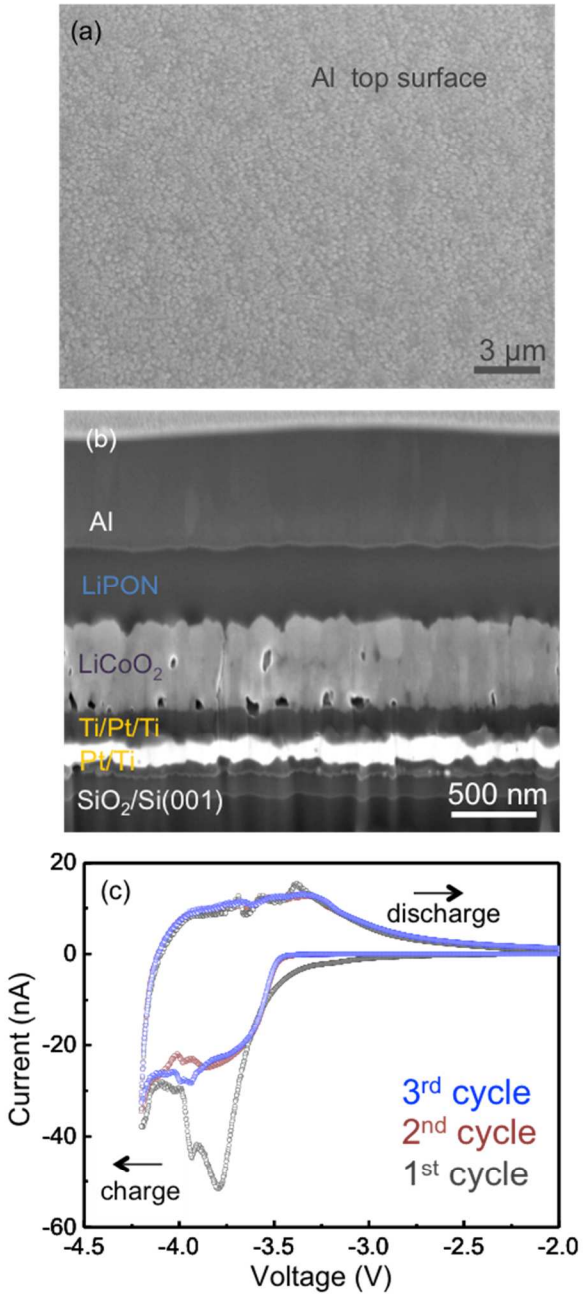

Figure 1: Al anode thin-film battery. (a) Plan view and (b) cross-section SEM images of a representative Al anode all solid-state thin-film battery before cycling. A very uniform and granular surface is originally obtained by the electron beam deposition of Al. (c) Cyclic voltammogram from -2.0 V to -4.2 V versus $LiCoO_2$ at a 0.15 mV/s scan rate for a representative battery. The first three cycles are shown. For the SEM images: (a) Detector: TLD, voltage: 5.0 keV, beam current: 100 pA, (b) Det: TLD, voltage: 5.0 keV, beam current: 50 pA.

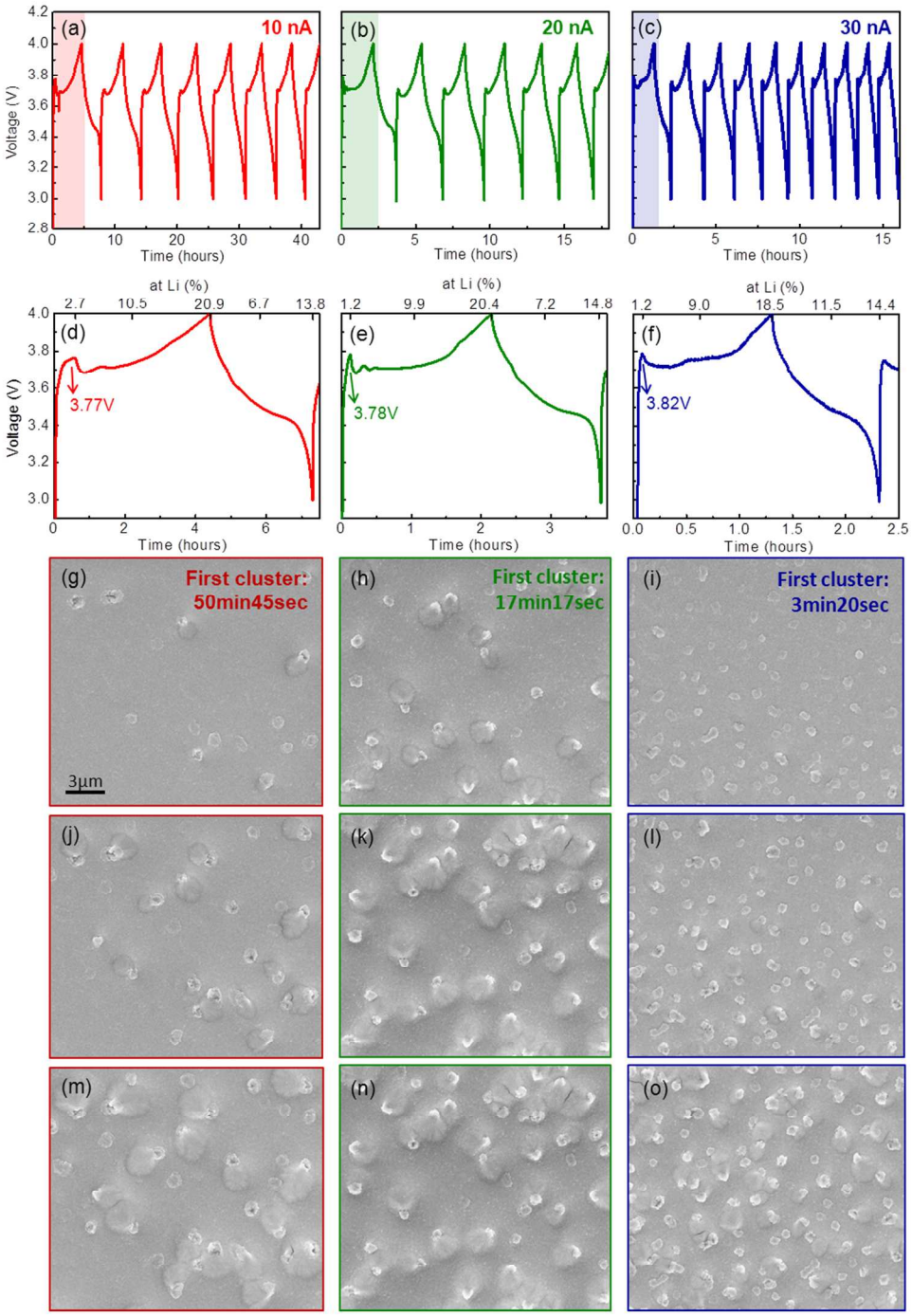

Figure 2: Al anode battery capacity loss. Galvanostatic cycling for battery at (a) 10, (b) 20, and (c) 30 nA. (d)-(f) Zoom in of galvanostatic cycling showing local voltage maxima, correspondent to the nucleation potential of the Al-Li clusters. (g)-(o) Plan view SEM images showing the morphology evolution of the Al anode surface for the first cycling step. By increasing the charging current, the density of clusters also increases, indicating that the Al-Li alloy formation is a kinetically driven process. For all SEM images: TLD detector, 5.0 keV, beam current: 100 pA.

Plan-view and cross-section SEM images of an as-fabricated battery with Al anode are shown in Figures 1a and b, where it can be seen that the amorphous LiPON layer conformally coats the $LiCoO_2$ layer without interfacial flaws. With these dimensions, each 0.5 mm TFLIB pad has a theoretical maximum cathode capacity of 0.0412 □Ah (21.2 □Ah/cm^2) and an anode theoretical capacity of 0.211 □Ah (107 □Ah/cm^2). The batteries were cycled in ultra-high vacuum (base pressure of 8.0 × 10^{-8} Pa) using a tungsten nanomanipulator probe as the top current collector and a

current-voltage generator to charge the device. Figure 1c shows a cyclic voltammogram (CV) from 2.0 V to 4.2 V versus Li/Li$^+$ at a 0.15 mV/s scan rate for a representative battery upon three full sweeps. A capacity of ≈20 □Ah/cm^2 is reached on the first charge cycle, or ≈94 % of theoretical cathode capacity and only ≈20 % of theoretical anode capacity.[15] However, the battery rapidly degrades, losing ≈90 % of its capacity after 100 cycles, as shown in Figure S2. Capacity loss is on discharge (i.e. the capacity measured during charging is nearly identical to the capacity measured during the previous discharge) indicating that Li is irreversibly trapped in the anode.

The first galvanostatic charge/discharge cycle collected at a current density of 15.3 □A/cm^2 is shown in Figure 3a. Figures 3b-i show SEM images of the Al anode surface recorded at the state-of-charge (SOC) and state-of-discharge (SOD) referenced to the Al anode indicated by the arrows in Figure 3a. The charge cycle shows a local maximum at 3.78 V (black arrow). Simultaneously, bright features nucleate at the surface of the anode. Similar batteries charged using different current densities exhibited the same behavior (see Figure 2). The voltage peak was initially associated with formation of AlLi.[16] More recently, however, *in situ* experiments of Y. Liu et al.[6] and Hudak et al.[10] provided convincing evidence that this dip in potential is due to formation of a Li-Al-O surface layer.[6,10,17,18] We thus associate the features nucleated on the surface with the formation of Li-Al-O$_x$. Upon further lithiation (Figures 3b – f), secondary features (mounds) with distinctly different contrast emerge from the side of the initial bright nucleation sites. These mounds increase in volume until a cell voltage of -4 V is reached (Figure 3f) (see video #1 in SI section).

During discharge most of the mounds contract due to delithiation of AlLi. With further cycling the anode area becomes increasingly covered with mounds, which impinge on each other, forming crack-like features at their boundaries. At this stage, the level of expansion/contraction of the AlLi mounds decreases substantially, as does the battery capacity.

To determine the structure of these features we used a Ga focused ion beam (FIB) to extract a cross-section of the batteries followed by TEM with selected area electron diffraction (SAED). Figure 4a shows a cross-section SEM image of a FIB-cut discharged battery after 10 charging cycles, while a similar cluster from the same battery is seen in a TEM bright-field image in Figure 4b with the corresponding SAED pattern shown in Figure 4c. The TEM images indicate that the mounds consist of nanometer-size randomly oriented grains of the AlLi *Fd3m* phase. There is no evidence of formation of other room temperature stable alloys, such as Li_3Al_2, Li_9Al_4,[19] and Li_2Al[20], which present a higher concentration of Li.

Another surprising finding revealed by TEM is that the bulk of the anode film remains fcc-Al (Figure 4d) without any evidence for reaction and no measurable Li, indicating that the lithiation process is primarily occurring at the surface. This behavior is in contrast to that observed for Si where microscopy reveals that reaction occurs throughout the anodes.[9] After 10 cycles, the morphology of the Al bulk remains the same but its thickness expands ≈ 16 % (Figure S1). Finally, cross-section FIB and TEM images provide no evidence that AlLi mounds lose electrical contact with the underlying bulk Al.

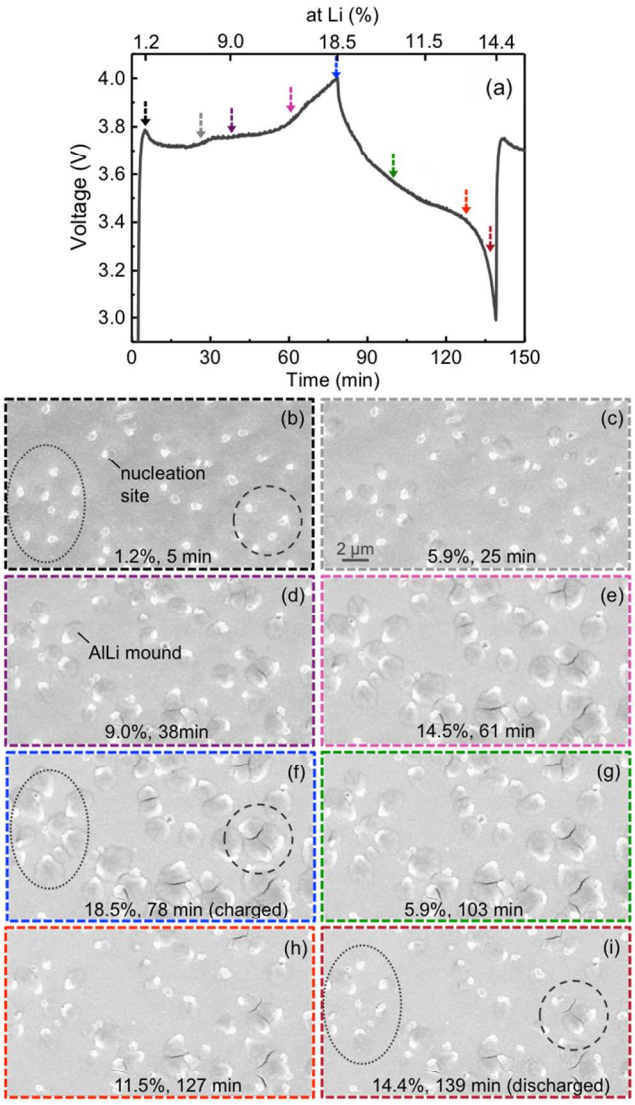

Figure 3. Battery morphology and electrochemical performance. (a) First galvanostatic charge-discharge cycle at 30 nA; arrows indicate time when sequence of plan view SEM images (b)-(i) were collected, showing Al-Li alloy evolution. For the SEM images: Detector: TLD, voltage: 5.0 keV, beam current: 100 pA. The Li percentage shown in the top y-axis of (a) refers to the atomic concentration of Li that diffuses during the charging and discharging cycles, respectively.

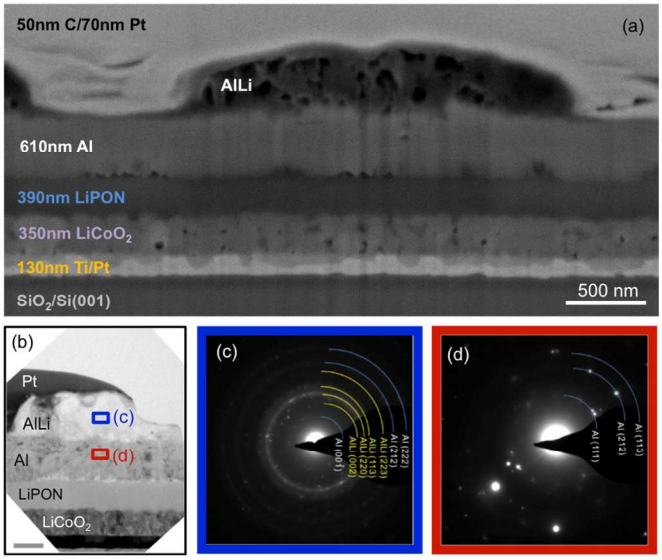

Figure 4. TEM analysis Al anode after lithiation. (a) Cross section SEM image of a battery after ten cycling sweeps showing an AlLi cluster formed at the Al anode's surface. A C/Pt layer is used to protect sample surface during focused ion beam milling. Detector: ICE, voltage: 5.0 keV, beam current: 50 pA, tilt: 52°. (b) TEM cross-section bright field. Scale bar is 250 nm. (c)-(d) SAED patterns from (b) collected at two different locations: (c) a mound on top of an Al layer containing the AlLi Fd3m phase, and (d) underneath it, showing pure Al.

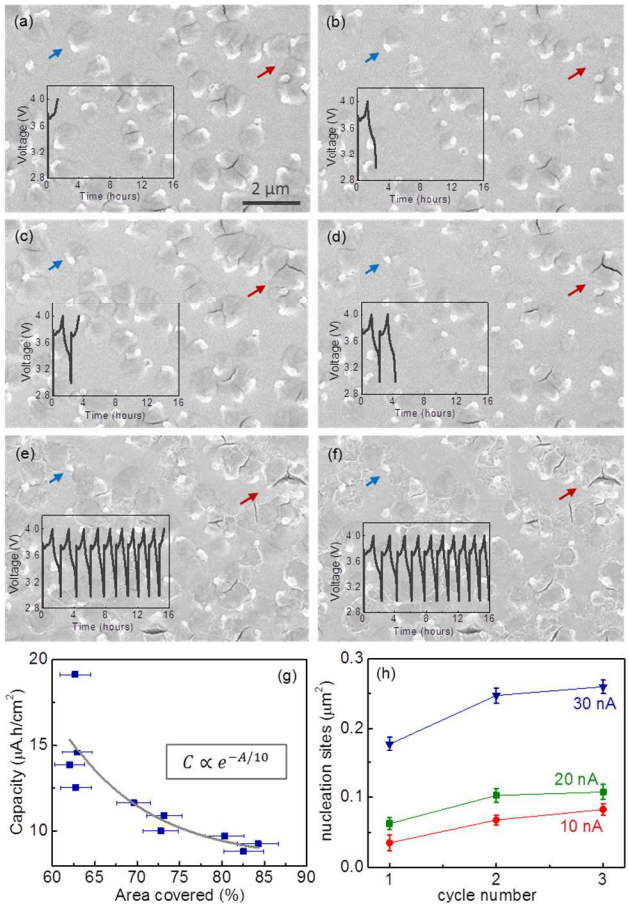

Figure 5. Sequence of in situ SEM images showing Al-Li alloy morphology evolution at the Al anode surface using 30 nA. After first (a) charging, (b) discharging, second (c) charging, (d) discharging, and tenth (e) charging, (f) discharging. Insets display real-time voltage profile measurements. The blue arrows show a cluster that is isolated, while the red arrows point to an ensemble of clusters that coalesce after the first charging cycle (c). Note that after ten cycles, the shape and size of the clusters remain approximately the same, as shown in (e) and (f). Detector: InLens, voltage: 5.0 keV, beam current: 100 pA. (g) Discharge capacity as a function of the percentage of the area covered by the cluster. Note the exponential decay of the capacity caused by irreversible lithiation, which saturates for ≈80 % of cluster coverage area. (h) Nucleation sites as a function of cycle number for similar batteries charged at different current values. In (g) and (h) the error bars indicate single standard deviation uncertainties and are primarily caused by uncertainty concerning the edges of the mounds and the number of craters per µm^2, respectively.

We now examine in more detail how the Al anode morphology evolves with increasing number of charge/discharge cycles and relate it to capacity loss. Figure 5 displays a sequence of *in situ* SEM images and the corresponding galvanostatic charge-discharge curves for ten cycles at 30 nA (1C-rate). After each cycle the mounds do not fully retract and the surface becomes increasingly covered with immobile mounds. When mounds impinge on each other, they form crack-like features at the boundaries and the degrees of expansion/contraction decrease sharply, see Figure S2. An obvious conclusion is that the trapped Li is contained in the immobile mounds as well as in the Li-Al-oxides, as suggested in [19]. This is quantitatively confirmed in Figure 5g where it is shown that immobile mound area closely tracks the capacity loss. Finally, Figure 5h shows that the density of nucleation sites slightly increases by cycling the battery independent of the amount of current used to charge the battery, as a result of the Li consumption by the mound.

At first glance it is puzzling why Li is trapped in the AlLi mounds since they seem to maintain electrical contact with the underlying Al film. However, for the AlLi mounds to form and decay requires the diffusion of *both* Al and Li. Li must diffuse through the film and Al must diffuse out of the film to be incorporated into the mound. Blockage of either of these diffusion channels would lead to capacity loss. In the following we present one scenario for how this might happen.

One scenario for the entrapment of Li is shown in Figure 6. The key point is that surface diffusion on Al can be sufficiently fast to cause large surface rearrangements at room temperature. For example the micron scale surface morphology of Al has been observed to change even below room temperature on less than hour time scales by Go *et al.* [21, 22] Therefore, a possible route for the AlLi mound formation is that Li makes its way to the Al surface. On the surface, Al diffusion would be sufficiently fast[23] that Al atoms can diffuse to the growing AlLi mounds and react with surface Li, increasing the mound volume.[22] This hypothesis is supported by the fact that Li diffuses ≈ 9 orders of magnitude faster into Si than it does in Al [24], probably resulting in the limited number of diffusion

pathways observed by SEM. Further, the formation of AlLi on the surface of the Anode film is due to our solid-state device configuration.

This scenario raises three questions: 1) Why doesn't the Li react with the Al when it first encounters it at the Al-LIPON interface? No long-range diffusion would be required. 2) What are the initial nucleation events observed before the mounds grow? 3) Why is the AlLi inside the mounds unable to dissociate during discharge after several cycles despite the thermodynamic driving force? An answer to the first question is that forming AlLi at the interface would necessarily create large stresses due to the volumetric expansion of AlLi in the absence of Al diffusion. As pointed out in Refs. [11, 12] these stresses would significantly impede nucleation and growth of AlLi phase. However, the AlLi mounds formed at the surface of the anode can be free of stress if a relatively small number of misfit dislocations are formed at the Al-AlLi interface, which is probably the case. An answer to both the second and third questions is that the original Al film surface is oxidized and not a good source of Al. (Extracting an Al atom through the Al_2O_3 lattice would require rearrangement of the oxide, which is unlikely because Al_2O_3 is very stable.) Therefore, Al is etched underneath the oxide layer close to the AlLi. This suggests that the nucleation and the growth of the AlLi mounds require nucleation of a void with an unoxidized surface in the interior of the film, underneath the Al_2O_3, which grows into the film as the AlLi mound evolves. The mounds seem to grow from the sides of the nucleated features on the surface. Perhaps the void nucleation is caused by Li initially reacting with the oxide to form a Li-Al-O glass as observed by Liu *et al*. in Al nanowires.[6] The volumetric expansion of the glass could lead to delamination of the oxide from the Al film to create a void with a clean surface.

This model supposes that AlLi grows underneath the oxide layer (Figure 6). Close inspection of the SEM images (see Supplemental material for real-time movies) indeed suggests that the mounds are growing underneath the original oxide (Figure 6a), because small surface features present on the original unreacted surface seem to persist on the AlLi mounds (Figure 6b). Pores in the AlLi phase would form during discharging for the same reason: Al must diffuse (even if diffusion of Li in AlLi is very fast) and the surface of the pores in the AlLi provide a pathway.[25]

Further support for the above scenario is provided by examining the chemical composition of the Al anode before, during, and after cycling characterize using Auger Electron Spectroscopy (AES). As expected for air exposed Al, the surface of the anode is covered with a few nanometer thick Al-oxide (Figure 7a). Reaction of Li with this oxide layer to form Li-Al-O_x provides a strong driving force for Li diffusion to the surface rather than reacting in the bulk where the associated strain energy impedes formation of AlLi. During cycling, more oxygen from the ambient is able to penetrate through microcracks into the porous AlLi mounds where the resulting surface oxide layer impedes surface diffusion paths. Evidence for continued oxidation of AlLi in the mounds is provided in Figure 7b, where we show that an AlO_x layer readily reforms on the surface of freshly sputtered Al films on a time scale of ~30 minutes and grows even faster during lithiation.

Dealloying AlLi at room temperature requires clean AlLi surfaces; exposure to oxygen or other ambient gases will passivate these reactive surfaces. It is possible that the apparent cracks in the SEM images are cracks in the oxide which have allowed the impurites to penetrate underlying pores and oxidize them, (Figure 6c). The intricate mound/pore morphology thus created is susceptible to degradation during charge-recharge cycles. It is important to note that Si thin film anodes used in solid state batteries do not experience this degradation mode.[8,26,27] The relative stability of Si anodes has a simple possible explanation: Si surface diffusion at room temperature is negligible, and thus the formation of surface mounds and the associated trapped Li does not occur. In fact, Li diffuses ≈ 9 orders of magnitude faster into Si than it does in Al.[24]

Conclusions

In summary, we quantified the anode degradation lithiation/de-lithiation processes by combining galvanostatic cycles with SEM images and AES under a controlled environment. The lithiation rate and the electrochemical potential were recorded and related with specific changes in the electrode morphology. Surprisingly, we found that significant changes in the Al film morphology occur at very low lithiation level. We showed that upon lithiation stable AlLi alloy mounds are formed on the top surface of the Al anode, as a result of the extremely low diffusivity of Li within Al and surface-driven reaction. Although these mounds remain in electrical contact with the Al, they do not disappear on discharge, leading to irreversible capacity loss. Additionally, we proposed a mechanism for the AlLi alloy formation irreversibility, based on surface oxidation of the AlLi and therefore, loss of Al diffusion paths. An alternative to minimize the capacity loss observed in this system is to modify the anode surface, in order to prevent the formation of the stable Al-Li-O alloy. The addition of a thin and inert metallic cap layer could prevent the surface driven reactions presented here. The direct *in situ* measurement of Li diffusion during lithiation/de-lithiation in an operating TFLIB represents an important step towards understanding and engineering the surface of Al and other metal anodes to improve capacity in rechargeable batteries.

Acknowledgements

The authors acknowledge N. Zhitenev, and N. Hudak for fruitful discussions, J. Schumacher for FIB-ed sample preparation for TEM measurements, and Nanofab at CNST. MSL and DR acknowledge support under the Cooperative Research Agreement between the University of Maryland and the National Institute of Standards and Technology Center for Nanoscale Science and Technology, award 70NANB10H193, through the University of Maryland. This work was partially supported by the Laboratory Directed Research and Development Program at Sandia National Laboratories. Sandia is a multi-program laboratory operated by Sandia Corporation, a Lockheed Martin Company, for the U.S. DOE National Nuclear Security Administration under Contract DE-AC04-94AL85000. NCB was supported by the DOE Office of Basic Energy Sciences, Division of Materials Science and Engineering. AAT acknowledges partial support for data analysis and writing of the manuscript by Science of Precision Multifunctional Nanostructures for Electrical Energy Storage (NEES), an Energy Frontier Research Center funded by the U.S. Department of Energy, Office of Science, and Office of Basic Energy Sciences under award DESC0001160.

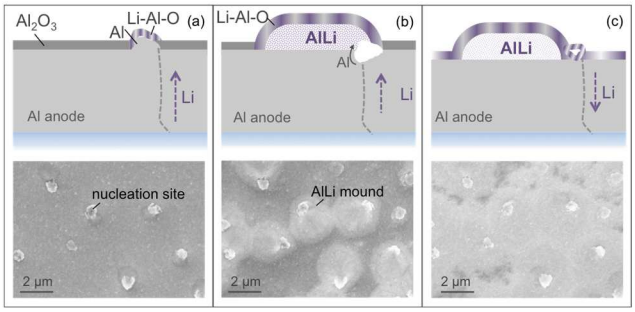

Figure 6. Schematic of lithiation/delithiation on Al anode thin-film batteries. (a) Lithium diffuses to the surface of the Al thin film to react with the Al_2O_3 surface oxide. Expansion of the lithiated Al_2O_3 creates a void with an unoxidized Al surface. (b) The surface of voids in the Al film provides a path for Al and Li to diffuse to a growing AlLi mound. As long as the voids remain unreacted this process is reversible. (c) Oxidation of the surface of the voids removes the diffusion paths for Al that is required for the facile decay of the AlLi mound. Layers are depicted out of scale for clarity. Bottom row shows plan view SEM images corresponding to each illustration (detector: TLD, 5.0 keV, beam current: 100 pA).

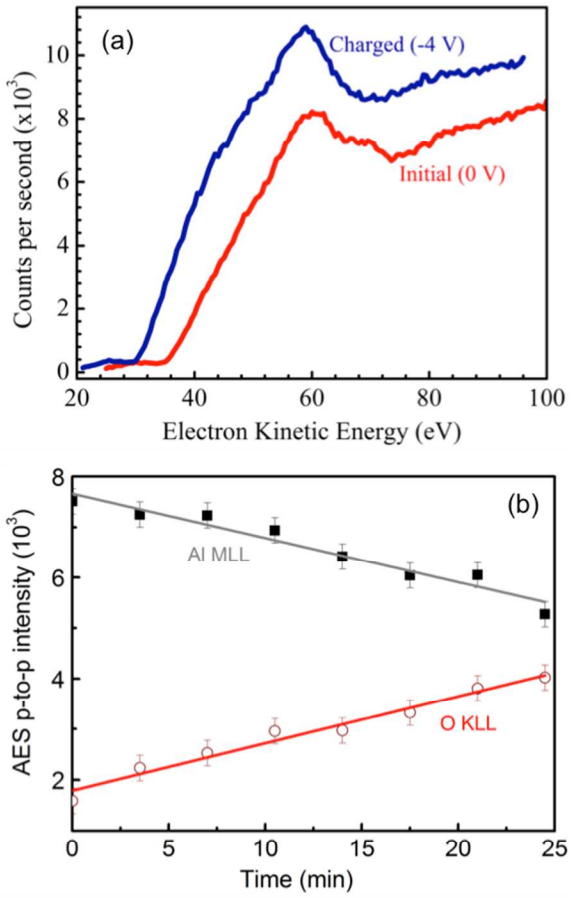

Figure 7. In situ spectroscopy of Al anode. (a) Auger electron spectrum of Al anode battery before and after cycling showing presence of oxygen even at the surface of a fresh device. (b) Time evolution of AlO_x layer regrowth on the surface of freshly sputtered Al films. Base pressure: 6.3×10^{-9} Torr.

Notes
[1]Department of Materials Science and Engineering, Institute for Research in Electronics and Applied Physics, College Park, MD 20742-2115, USA
[2]Center for Nanoscale Science and Technology, NIST, Gaithersburg, MD, USA
[3]Maryland NanoCenter, University of Maryland, College Park, MD, 20899-6204, USA
[4]Material Measurement Laboratory, NIST, Gaithersburg, MD, USA
[5]Sandia National Laboratories, Livermore, CA, USA

Electronic Supplementary Information (ESI) available: including additional figures and movies showing anode morphology change upon battery cycling. See DOI: 10.1039/b000000x/

References

1. A. R. Jha, *Next-Generation Batteries and Fuel Cells for Commercial, Military, and Space Applications*, CRC Press, 2012.
2. J. M. Tarascon and M. Armand, *Nature*, 2001, **414**, 359-367.
3. M. Armand and J. M. Tarascon, *Nature*, 2008, **451**, 652-657.
4. M. J. W. Lindsay, G. X.; Liu, H. K., *Journal of Power Sources*, 2003, **119**, 84-87.
5. H. Li, Z. X. Wang, L. Q. Chen and X. J. Huang, *Advanced Materials*, 2009, **21**, 4593-4607.
6. Y. Liu, N. S. Hudak, D. L. Huber, S. J. Limmer, J. P. Sullivan and J. Y. Huang, *Nano Letters*, 2011, **11**, 4188-4194.
7. X. H. Liu, J. W. Wang, S. Huang, F. F. Fan, X. Huang, Y. Liu, S. Krylyuk, J. Yoo, S. A. Dayeh, A. V. Davydov, S. X. Mao, S. T. Picraux, S. L. Zhang, J. Li, T. Zhu and J. Y. Huang, *Nature Nanotechnology*, 2012, **7**, 749-756.
8. S. W. Kim, D. H. Seo, X. H. Ma, G. Ceder and K. Kang, *Advanced Energy Materials*, 2012, **2**, 710-721.
9. U. Kasavajjula, C. S. Wang and A. J. Appleby, *Journal of Power Sources*, 2007, **163**, 1003-1039.
10. N. S. Hudak and D. L. Huber, *Journal of the Electrochemical Society*, 2012, **159**, A688-A695.
11. T. Ichitsubo, S. Yagi, T. Doi, S. Yukitani, K. Hirai and E. Matsubara, *Journal of the Electrochemical Society*, 2012, **159**, A14-A17.
12. T. Ichitsubo, S. Yukitani, K. Hirai, S. Yagi, T. Uda and E. Matsubara, *Journal of Materials Chemistry*, 2011, **21**, 2701-2708.
13. X. H. Liu, Y. Liu, A. Kushima, S. L. Zhang, T. Zhu, J. Li and J. Y. Huang, *Advanced Energy Materials*, 2012, **2**, 722-741.
14. D. Ruzmetov, V. P. Oleshko, P. M. Haney, H. J. Lezec, K. Karki, K. H. Baloch, A. K. Agrawal, A. V. Davydov, S. Krylyuk, Y. Liu, J. Y. Huang, M. Tanase, J. Cumings and A. A. Talin, *Nano Letters*, 2012, **12**, 505-511.

15. R. Wartena, A. E. Curtright, C. B. Arnold, A. Pique and K. E. Swider-Lyons, *Journal of Power Sources*, 2004, **126**, 193-202.
16. Y. S. M. C. Y. Wang, G. Ceder, and Y. Li, *J. Electrochem. Soc.* , 2008, **155**, A615-A622.
17. J. Song, X. Yang, S. S. Zeng, M. Z. Cai, L. T. Zhang, Q. F. Dong, M. S. Zheng, S. T. Wu and Q. H. Wu, *Journal of Micromechanics and Microengineering*, 2009, **19**.
18. W.-J. Zhang, *Journal of Power Sources*, 2011, **196**, 13-24.
19. B. Hallstedt and O. Kim, *International Journal of Materials Research*, 2007, **98**, 961-969.
20. K. Puhakainen, M. Bostrom, T. L. Groy and U. Haeussermann, *Journal of Solid State Chemistry*, 2010, **183**, 2528-2533.
21. E. P. Go, K. Thuermer and J. E. Reutt-Robey, *Surface Science*, 1999, **437**, 377-385.
22. W. Gasior and Z. Moser, *Scandinavian Journal of Metallurgy*, 2002, **31**, 353-358.
23. C. Moreau, A. Allouche and E. J. Knystautas, *Journal of Applied Physics*, 1985, **58**, 4582-4586.
24. G. A. Tritsaris, K. Zhao, O. U. Okeke and E. Kaxiras, *Journal of Physical Chemistry C*, 2012, **116**, 22212-22216.
25. M. J. A. Jonah Erlebacher, Alain Karma, Nikolay Dimitrov, and Karl Sieradzki, *Nature*, 2001, **410**, 450-453.
26. A. Seeger, D. Wolf and H. Mehrer, *Physica Status Solidi B-Basic Research*, 1971, **48**, 481.
27. V. P. Phan, B. Pecquenard, and F. Le Cras, *Advanced Functional Materials*, 2012, **22**, 2580–2584.

